Article

Bandgap Engineering and Enhancing Optoelectronic Performance of a Lead-Free Double Perovskite $Cs_2AgBiBr_6$ Solar Cell via Al Doping

Asad Ullah, Muhammad Iftikhar Khan,* Ihtisham-ul-haq, Badriah S. Almutairi, Dalil Bulayis N. AlResheedi, and Jeong Ryeol Choi*

Read Online

ACCESS | Metrics & More | Article Recommendations

ABSTRACT: In this study, solar cells based on pure $Cs_2AgBiBr_6$ and Al-doped metal were fabricated using the sol−gel spin-coating technique. X-ray diffraction (XRD) analysis confirmed the formation of cubic-structured films for both pure and Al-doped. Notably, the grain size of Al-doped $Cs_2AgBiBr_6$ was observed to be larger than that of its pure counterpart. The optical properties of these films were investigated using UV−vis spectroscopy, revealing essential parameters such as the bandgap energy (E_g), refractive index (n), extinction coefficients (k), and dielectric constant. While the pure film exhibited an E_g of 1.91 eV, the Al-doped film demonstrated a slightly lower E_g of 1.82 eV. Utilization of these films in solar cell fabrication yielded intriguing results. The $J−V$ curve shows that the pure solar cell displayed a short-circuit current density (J_{sc}) of 5.01 mA/cm², a fill factor (FF) of 0.67, an open-circuit voltage (V_{oc}) of 0.89 V, and an efficiency of 3.02%. Al doping led to improvements, with an increase in V_{oc} to 0.91 V, FF to 0.71, and J_{sc} to 5.29 mA/cm². Consequently, the overall efficiency surged to 3.40%, marking a substantial 12.5% enhancement compared with the pure solar cell. These findings underscore the efficacy of Al doping in enhancing the performance of $Cs_2AgBiBr_6$-based solar cells.

1. INTRODUCTION

The need for energy is growing worldwide, and as fossil fuels become scarcer, there is a noticeable movement in favor of obtaining alternate energy sources, particularly when it comes to environmentally friendly energy options.[1,2] For a number of reasons, solar energy has become a popular substitute for fossil fuels. It is an essential part of the switch to renewable energy sources because of its abundance, advantages for the environment, affordability, and potential for energy independence.[3−5] As a consequence, solar energy, harnessed through photovoltaic technology, has become a leading contender as a clean and sustainable alternative to fossil fuels. In particular, metal halide perovskites have gained significant attention and interest in recent years.[6,7] Metal halide perovskites, described by the general chemical formula ABX_3, was considered: A cations here is a choice between $CH_3NH_3^+$ (MA^+), $CH(NH_2)^{2+}$ (FA^+), or Cs^+ (cesium), B cations as Pb^{2+}, and X anions as Cl^-, Br^-, or I^-.[8−10] Perovskite solar cells (PSCs) exhibit exceptional performance due to their unique characteristics, which include a high absorption coefficient, a direct and modifiable bandgap, balanced electron and hole transport, an extended carrier diffusion length, and favorable charge carrier mobilities.[11] Furthermore, PSCs show a great deal of promise when used in place of traditional solar devices. In a few years,

PSCs' power conversion efficiency (PCE) increased significantly, from 3.8 to 22.1%.[12,13] On the other hand, lead halide perovskites' instability and the ongoing problems with health and the environment have made commercialization difficult. These shortcomings are primarily associated with the leaching of Pb^{2+} ions due to their water solubility.[14,15] Less toxic ions such as Sn^{2+}, Bi^{3+}, Ge^{2+}, Sb^{3+}, Mn^{2+}, and Cu^{2+} offer a promising alternative to Pb^{2+} in perovskites, allowing for the creation of new lead-free perovskite structures. The incorporation of these metal cations not only broadens the range of perovskite variants but also promotes the development of PSCs in an environmentally friendly way.[16,17] The fact that these solar cells have shown reduced PCE in comparison to Pb-based perovskite cells is noteworthy. The discovery of Pb-free halide double perovskites (LFHDPs), which have the chemical formula $A_2B'B''X_6$, has recently led to the possibility of a
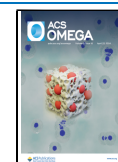
solution. In LFHDPs, two bivalent metallic Pb^{2+} cations are substituted with one monovalent and one trivalent cation, leading to a modification in the dimensionality within the crystal structure.[18,19] Because of its versatility in terms of composition and structure, multiple cation substitution is acknowledged as one of the most effective methods within the context of LFHDPs. The Goldschmidt tolerance factor (GT) and octahedral factors (OF) play essential roles in the quest for appropriate and stable perovskite structures.[20] Among the LFHDPs under examination, only a limited number of perovskite materials have met the necessary criteria for integration into solar cell applications. Significantly, $Cs_2AgBiBr_6$ has become one of the most widely adopted absorbers in LFHDP solar cells.[20−22]

The above-mentioned consequence for $Cs_2AgBiBr_6$ is primarily attributed to its notable characteristics, including a high carrier lifetime, relatively small carrier effective mass, strong moisture stability, and low toxicity. While $Cs_2AgBiBr_6$ solar cells have demonstrated a modest power conversion efficiency (PCE) of around 3%, they exhibit highly promising exceptional physicochemical properties such as extended carrier lifetimes, robust elasticity, resistance to thermal expansion, long-term stability, and nontoxicity.[23−25] However, $Cs_2AgBiBr_6$ also shows several disadvantages, including the presence of prominent surface imperfections, the extensiveness of the electron−phonon interaction, the presence of excitons, and difficulties in the manufacturing process, which are particular issues related to low solubility and the requirement for high-temperature phases.[20,26] Despite comprehensive efforts aimed at enhancing solar cell architectures with the film formation and preparation for this material, the efficiency has only managed to reach 2.4%.[27,28] The limited efficiency primarily results from the wide bandgap and weak light absorption, while the latter issue arises from the material's indirect bandgap. To address this challenge, it is necessary to modify the band structure of the material.[29−31] Multiple effective strategies have been devised to boost the performance of LFHDPs, including partial substitution at the A-site, B-site, or B″-site, chemical substitution, and the incorporation of heterostructure interfaces. Among these approaches, doping stands out as especially well-suited due to its simplicity and straightforward implementation. Furthermore, it offers the advantage of adjusting the LFHDP properties without the need to alter the crystal structure. To tackle the aforementioned difficulties, Al doping into $Cs_2AgBiBr_6$ has been carried out. Because of its capacity to improve stability, lower the bandgap, and increase conductivity, all of which ensure that films have enhanced electrical and optical properties, Al doping has attracted a lot of attention. Furthermore, doping effectively reduces the annihilation of electron−hole pairs, leading to the presence of free electrons in the conduction band and consequently lowering electrical resistance.[32−36] Additionally, Al doping encourages grain elongation. This increase in grain sizes in perovskite films is associated with increased crystallinity, which is a desirable property for reducing flaws and enhancing the stability of perovskite-based devices. The improved crystalline structure is essential for improving charge transfer in the perovskite layer, which is necessary to increase the solar cell efficiency. Larger grains are advantageous for charge.[37−39]

This work presents a novel examination into effective Al integration into $Cs_2AgBiBr_6$, a promising LFHDP material. Comprehensive characterizations using UV−vis spectroscopy,

solar simulator measurements, and X-ray diffraction (XRD) were performed on produced Al-doped $Cs_2AgBiBr_6$. The material's crystalline structure and phase purity were clarified by the XRD investigation, which also shed light on how Al doping affected the perovskite lattice. The optical properties were investigated using UV−vis spectroscopy, which showed variations in the absorption spectra that were suggestive of moderation in the electronic system. In addition, experiments using a solar simulator were carried out to evaluate the photolysis efficiency and execution of Al-doped $Cs_2AgBiBr_6$ as a possible photovoltaic application candidate. A thorough grasp of the constructional, optical, and photo offset characteristics of the new Al-doped $Cs_2AgBiBr_6$ is provided by the combined use of various characterization approaches, which makes a significant contribution to the developing field of LFHDP materials for sustainable energy technologies.

2. EXPERIMENTAL SECTION

Like other perovskite materials, double perovskites are susceptible to light, oxygen, and moisture in the environment. The limited solubility of the precursors needed for the production of $Cs_2AgBiBr_6$, a type of double perovskite, makes it difficult to fabricate high-quality films; therefore, the synthesis of this material is usually not done in ambient air. The fabrication of $Cs_2AgBiBr_6$ films is done under high vacuum conditions. This helps to achieve double perovskite $Cs_2AgBiBr_6$ films with excellent crystallinity, flatness, and absence of pinholes. The process often involves annealing at high temperatures (at least 280 °C) in a controlled atmosphere, such as a nitrogen-filled glovebox. This helps to fully convert the precursors into $Cs_2AgBiBr_6$ and obtain high-quality films.[27,40,41]

Bismuth bromide ($BiBr_3$, 98%) and cesium bromide (CsBr, 99.9%) were obtained from Sigma-Aldrich. Sigma-Aldrich was also the source of isopropanol (IPA, 99.5%), hydroiodic acid (HI, 57 wt % in H2O, 99.95%), dimethyl sulfoxide (DMSO, anhydrous, 99.8%), and chlorobenzene (CB, 99.8%). We bought silver bromide (AgBr, 99.998%) from Alfa-Aesar. Greatcell Solar Materials provided the formamidinium iodide (FAI, >99.99%), guanidinium iodide (GAI, >99%), and methylammonium iodide (MAI, >99.99%). None of the solvents needed to be further purified before use. The resulting composition was stirred at 120 °C until the solvents evaporated, leaving behind crimson-hued crystals. Maxing was halted, and then gradually cooled with an hourly rate of 5 °C. The set of components was then left undisturbed for an entire night. Following their precipitation, the red crystals were separated and collected by filtration. Following this, they underwent an ethanol wash. The resulting solid product was dried in a vacuum at 60 °C, yielding the development of $Cs_2AgBiBr_6$ crystals. The same process was repeated for Al doping, with 5% Al incorporated with every chemical constituent. Particle size and phase composition of pure and Al-doped $Cs_2AgBiBr_6$ films were examined through XRD analysis. XRD was conducted using a Panalytical Empirian diffractometer configured in the Bragg−Brentano setup, employing Cu Kα radiation (λ = 1.54 Å), within the range of 2θ = 10−70°. The absorption spectra were acquired using a Shimadzu UV−vis spectrophotometer UV-2600 to further investigate the optical properties of the materials.

To create a precursor solution for both pure $Cs_2AgBiBr_6$ and Al-doped variants, initially dissolved in 1 mL of DMSO solvent, AgBr (0.5 mg, 93.9 mmol), CsBr (1.0 mg, 212.8 mg),
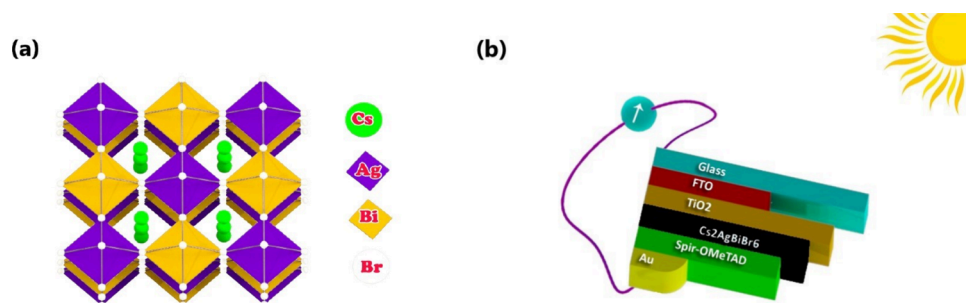
Figure 1. (a) Schematic diagram of crystal structure of double perovskites. (b) Step-by-step coating of layers: FTO, TiO$_2$, perovskite, spiro-OMeTAD, and Au.
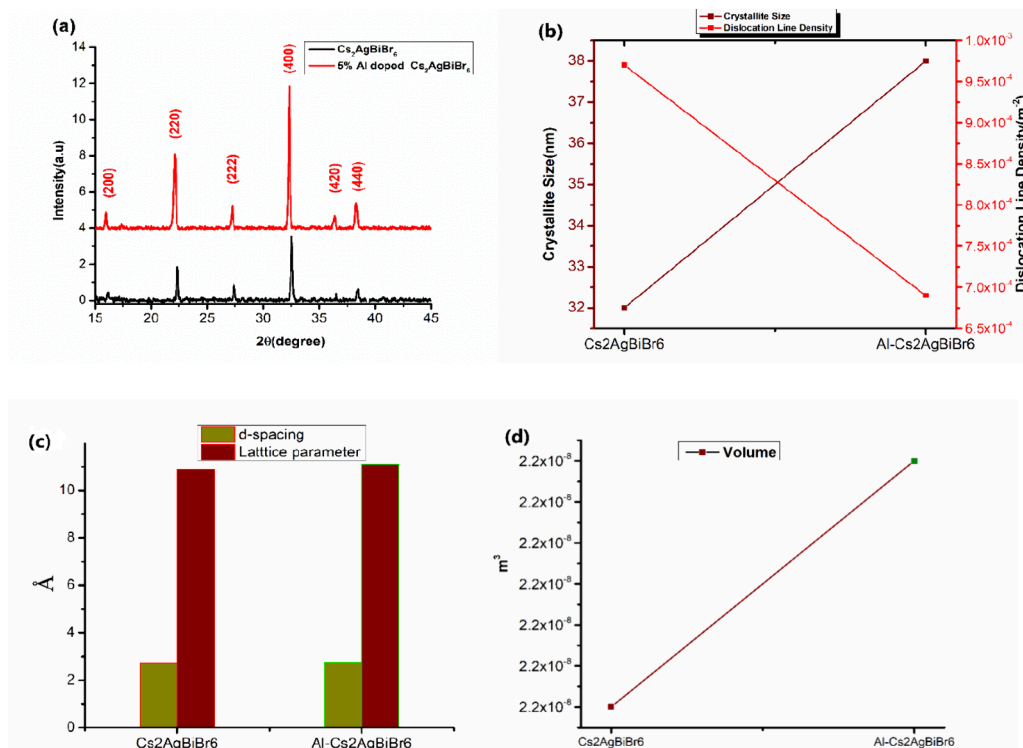

Figure 2. (a) XRD pattern for undoped and Al-doped Cs$_2$AgBiBr$_6$ halide double perovskite solar cell and zoom-in for clear vision of shifting of 2θ degree of the (400) plane. (b) Crystallite size and dislocation line density of undoped and doped. (c) d-Spacing and lattice parameter. (d) Volume of pure and doped.

and BiBr$_3$ (0.5 mmol, 224.3 mg) were combined. Subsequently, the mixture was subjected to heating at 75 °C for several hours, ultimately resulting in the development of a light-yellow mixture. The deposition of the Cs$_2$AgBiBr$_6$ and Al-doped films was carried out by using the spin-coating method. Specifically, 100 μL of these mixtures were applied via spin-coating onto the glass/FTO/TiO$_2$ layers at a rotational speed of 3000 rpm for a duration of 1 min. To achieve the generation of the double perovskite phase, the resulting film was heated up for 5 min at 280 °C. The construction of solar cells utilizing these films was performed on TiO$_2$/FTO/glass substrates, following the fabrication method previously detailed in our earlier work.[42]

To produce the hole transport material (HTM), an initial solution (A) was prepared by combining 36 mL of tributylphosphate (TBP). Using 22 mL of a prepared solution that contained 520 mg/mL lithium bis-trifluoromethyl sulfonyl imide. Within solution (A), we introduced and stirred 72 mg of spiro-OMeTAD. This process resulted in the development of a

solution, now termed as solution (B). To create the final solution, we incorporated 1.0 mL of chlorobenzene into solution (B). To better the photoactive layer's wettability, extend the performance duration, and enhance the device's connectivity, we coated the electrode with an 80 nm-thick layer of gold using an external source. These solar cells featured an active area measuring 0.16 cm^2. As shown in Figure 1b, the solar cell's layer configuration was as follows: glass/FTO/TiO$_2$/Cs$_2$AgBiBr$_6$/spiro-OMeTAD/Au. A solar simulator with a calibrated air mass (AM) of 1.5 G and an intensity of 100 mW/cm^2 was used to test the solar cells. Another feature of the testing gear was a computer-controlled source meter, a Keithley 2400 (produced by Keithley Instruments, Inc., Cleveland, OH, USA). The J−V curve was produced with this configuration. The voltage sweep was carried out between 1.2 and 0 V in the reverse bias direction. The device was tested with an AM of 1.5 and standard 1 sun illumination. The voltage sweep was carried out at a scan rate of 0.2 V/s.[43]

3. RESULTS AND DISCUSSION

3.1. Structural Analysis. The XRD analysis shows that the synthesized material consists entirely of the pure-phase $Cs_2AgBiBr_6$, with no traces of any other secondary phases, as depicted in Figure 2a. $Cs_2AgBiBr_6$ possesses crystallizes in a cubic elpasolite structure with Fm3m symmetry.[44] These parameters closely match those found in the standard JCPDS data with the file number (01-084-8699). The presence of all odd Miller indices in the XRD pattern suggests that Ag^+ and Bi^{3+} ions exhibit a rock salt ordering within the structure. The lattice parameter for $Cs_2AgBiBr_6$ is approximately equal to a = 10.9 Å, but for doping of Al, its value becomes 11.1 Å, which is consistent with the values reported in the literature.[8] The primary peaks in the XRD pattern for pure $Cs_2AgBiBr_6$ were analyzed at 2θ angles of 16.1, 22.3, 27.3, 32.6, 36.4, and 38.4°, corresponding to the crystallographic indices (hkl) of (200), (220), (222), (400), (420), and (440), respectively, as shown in Figure 2a. Observation from the XRD pattern revealed that these peaks exhibited a slight shift toward a lower angle by Al doping. The main peak of (400) at 32.6° for pure was shifted by doping leftward, resulting in 32.2° showing a difference of 0.4°. This shift in peak positions results in a decrease in 2θ which implies an expansion of the interplanar spacing (d-spacing) between the crystal lattice planes.[38] The observed shift in the peaks serves as evidence of the successful doping of Al into $Cs_2AgBiBr_6$, and no additional phases or Al-related peaks were detected, confirming the material's purity. It can also be seen that the intensity of the peaks is enhanced by doping, which is in correspondence with the crystallinity of the material. By increasing the intensity of the peaks, the strain is produced in the crystal lattice because of the insertion of the $Al(3p^1)$.[45]

Ag and Bi alternately occupy the cores of the octahedra in all three orientations with Cs^+ occupying the central position within the cuboctahedral cavity. This arrangement results in a supercubic structure, as illustrated in Figure 1a. Furthermore, inverted planar heterojunction perovskite solar cells (PSCs) were fabricated with the device structure glass/FTO/TiO_2/$Cs_2AgBiBr_6$/spiro-OMeTAD/Au as shown in Figure 1b. To enable interparticle electron transfer and close contact between the two polymorphs is necessary. The critical factor for this intimate contact lies in their crystallite size. The crystallite size can be calculated by the Scherrer equation[46]:

$$D = \frac{K\lambda}{\beta \cos \theta} \quad (1)$$

where K is a constant. The eq 1 establishes a connection between the crystallite size (D) and various attributes of the diffraction peak such as the wavelength of the X-ray beam (λ), the full-width at half-maximum (fwhm) of the peak (β), and the Bragg angle (θ). The peaks (400) and (220) were chosen for crystallite size measurement considering their high intensities. Consequently, the crystallite size for the pristine $Cs_2AgBiBr_6$ measures 32 nm, whereas for the doped materials, it extends to 38 nm as shown in Figure 2b. Hence, it can be concluded that the increase in crystallite size is due to the Al dopant having a greater ionic radius than the host Ag. Dislocation line density is a crucial parameter employed for assessing the existence and concentration of dislocations within a crystalline material. The unit of measurement for dislocation line density is expressed as m/m³ and given by the relation[47]:

$$\delta = 1/D^2 \quad (2)$$

The dislocation line density for the pristine material is 9.7×10^{-4}, while for the doped material, it is reduced to 6.9×10^{-4} as shown in Figure 2b. This decrease in dislocation density with Al doping in $Cs_2AgBiBr_6$ films may be attributed to the difference in ionic sizes between Al^{3+} and Ag^+ within the $Cs_2AgBiBr_6$ lattice which increases crystal perfection.[48] A crucial quantity in X-ray diffraction analysis, interplanar d-spacing (d), is used to determine the crystal structure of a material. The 'd' signifies the perpendicular distance between two consecutive crystallographic planes of atoms within a crystal lattice. In the context of the Al-doped $Cs_2AgBiBr_6$ double perovskite, the values of this 'd' can be computed from the diffraction peak positions (2θ) corresponding to various diffraction planes (hkl) utilizing Bragg's law[49]:

$$d = n\lambda/2\sin \theta \quad (3)$$

It is a well-established fact that diffraction peaks undergo displacement and broadening under stress or strain effects. For undoped $Cs_2AgBiBr_6$, the measured d-spacing for the most intense reflection (100%) at a 2θ value of 32.6 peaks in the observed powder patterns was 2.74 Å. Upon doping, a slight shift in this d-spacing to 2.77 Å was detected. Given the lack of significant displacement, we infer that the dopant's strain is negligible. Our calculation of crystallite size using Scherrer's line broadening can be justified as depicted in Figure 2b, where the d-spacing values are presented in Figure 2c. This increase in 'd' suggests a change in the crystal lattice. It is worth noting that the lattice parameter (a) is found to increase in the order of F < Cl < Br-based double perovskites. This increase can be attributed to the enlargement of atomic size.[50] Furthermore, the increase in the lattice parameters following 5 wt % Al doping is attributed to the films experiencing tensile strain along their c-axis. Additionally, the doping of 5 wt % which was not detected in XRD might induce a change in the 'a' value.[51,52] Lattice parameter and volume can be calculated by formulas:

$$a^2 = (h^2 + k^2 + l^2)d^2 \quad (4)$$

$$\text{Volume} = a^3 \quad (5)$$

The 'a' value for pure $Cs_2AgBiBr_6$ was 10.9 Å after doping its value increased to 11.1 Å as shown in Figure 2c. The lattice parameters of the samples were determined by selecting diffraction peaks from the crystal planes (220), (222), and (400). The alterations in lattice parameters due to doping manifested as a slight elongation of the 'c'-axis, while "a" and "b" remained nearly constant. As only the 'c' parameter exhibited marginal changes, it can be inferred that the dopants occupied both bcc and fcc positions within the structure.[53] The volume for pure was 2.20×10^{-8} m³, and for doped, it becomes 2.23×10^{-8} m³ as shown in Figure 2d. The distinction in structural properties between the pristine and 5% Al-doped $Cs_2AgBiBr_6$ double perovskites is evident. The expansion in the d-values for the Al-doped $Cs_2AgBiBr_6$ double perovskites, compared to the undoped counterpart, serves as clear evidence of the successful incorporation of Al into the $Cs_2AgBiBr_6$. By introducing Al^{3+} through doping, it is possible that the $[BiBr_6]^{-3}$ octahedra in the $Cs_2AgBiBr_6$ double perovskite lattice could be replaced by $[TiBr_6]^{-3}$ octahedra. This substitution is attributed to the notable electronegativity gap between Al (1.61) and Cs (0.79), in addition to the charge disparity between Al^{3+} and Cs^+.
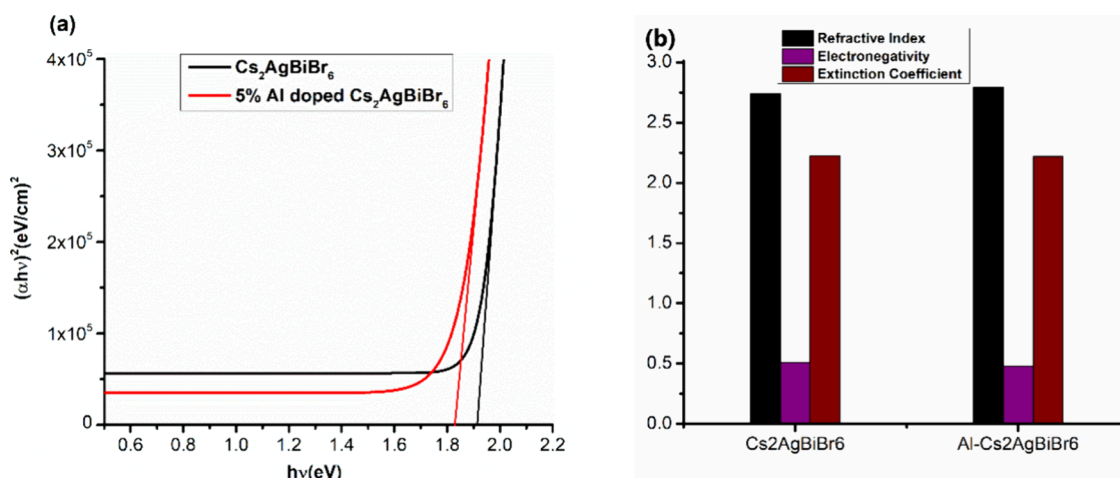
Figure 3. (a) E_g of pure and Al-doped $Cs_2AgBiBr_6$ films and (b) refractive index, optical electronegativity, and extinction coefficient of pure and doped $Al-Cs_2AgBiBr_6$.

However, the replacement of Cs by Ag ions in the $Cs_2AgBiBr_6$ lattice is unlikely due to the differences in the electronegativity and charge. Conversely, the electronegativity of Al (1.61) is relatively similar to those of Ag (1.93) and Bi (2.0), and there is a charge whose equilibrium is more effectively maintained by Bi^{3+} and Al^{3+} as compared to Bi^{3+} and Ag^+. Consequently, it is expected that the substitution of $[TiBr_6]^{-3}$ octahedra for $[BiBr_6]^{-3}$ octahedra is a more dominant process in the formation of the Al-doped $Cs_2AgBiBr_6$ lattice.[54]

3.2. Optical Analysis. To calculate the bandgap energy (E_g) of both the pure $Cs_2AgBiBr_6$ and Al-doped films, a graph was generated by plotting ($\alpha h\nu$) against the energy of photons ($h\nu$), as depicted in Figure 3a. In this figure, α quantifies the light absorption, ν represents the frequency of light, and h symbolizes Planck's constant. The bandgap energy is determined using Tauc's relation[55,56]:

$$\alpha h\nu = A(h\nu - E_g)^n \tag{6}$$

where 'n' is a numerical factor and 'A' is a constant of proportionality. The exponent in this equation is typically represented as $n = 1/2$ for the materials that exhibit direct allowed transitions. The optical bandgap of the pristine $Cs_2AgBiBr_6$ was 1.91 eV, consistent with previously reported values for $Cs_2AgBiBr_6$.[57] In contrast, E_g of the Al-doped $Cs_2AgBiBr_6$ was determined to be 1.82 eV as calculated from the UV−vis spectroscopy result shown in Figure 3a, signifying a significant reduction in bandgap when compared to the undoped film. This suggests that Al doping offers a more versatile means of tuning the bandgap, subsequently altering the electronic structure and optical properties. Reducing the bandgap is crucial in solar cells as it enhances the absorption of photons within the solar spectrum. This enhancement results in a higher photocurrent production by the cell.[58−60] At the same time, the increased interaction between Al-3p and Ag-5s states results in a broader conduction band, causing the density of states to shift toward lower energy levels. In the case of Al-doped $Cs_2AgBiBr_6$, this shift leads to the upward movement of the Fermi level into the conduction band, facilitating the formation of an n-type semiconductor. This adjustment eases optical transitions and enhances the overall optical characteristics of the material.[61,62] Therefore, the Al doping introduces new energy levels into the bands of $Cs_2AgBiBr_6$ subsequently

reducing the bandgap between the valence and conduction bands in thin films of $Cs_2AgBiBr_6$.

The refractive index (n) is a critical physical parameter that directly correlates with the atomic interactions at the microscopic level.[61,63] The n for both pure and Al-doped thin films was determined through the following equation:

$$n = \sqrt{1 + \left(\frac{A}{E_g + B}\right)^2} \tag{7}$$

where A and B are constants having values 13.6 and 3.4 eV, respectively. The value (n) for pristine $Cs_2AgBiBr_6$ was 2.74 and the value of doped Al increased to 2.79 as shown by the graph in Figure 3b. The rise in the refractive index 'n' can be attributed to a reduction in the bandgap resulting from Al doping causing the medium to become denser. Consequently, light is bent more significantly, indicating increased light scattering, which is advantageous for solar cells[64,65]. This increase in 'n' also corresponds to high polarizability associated with larger atomic radii. Notably, the 'n' achieves its maximum value within the visible region for these compounds, which suggests their promising prospects for use in optoelectronic applications. The rise in the 'n' of $Cs_2AgBiBr_6$ thin films may be attributed to the increased film densification and pore filling resulting through the Al doping process.[66,67]

Electronegativity is a property of an element or atom that reflects its tendency to attract electrons. It provides important insights into the nature of chemical bonding and the type of bond that forms between two atoms. The Pauling scale is a commonly used scale for electronegativity values. When the electronegativity difference (ΔEN) between two atoms is in the range of 0.5−1.6, the bond connecting them is categorized as a polar covalent bond. In a polar covalent bond, the electrons are not shared equally between the atoms, and there is an uneven distribution of charge leading to partial positive and partial negative charges on the atoms. A nonpolar covalent bond usually occurs when the electronegativity difference is less than 0.5. In nonpolar covalent bonds, the electrons are shared almost equally between the atoms, resulting in a symmetrical distribution of the charge. In the presence of a metal, the bond transitions into an ionic one when the electronegativity difference between the metal and nonmetal exceeds 1.6. In an ionic bond, electrons are transferred from
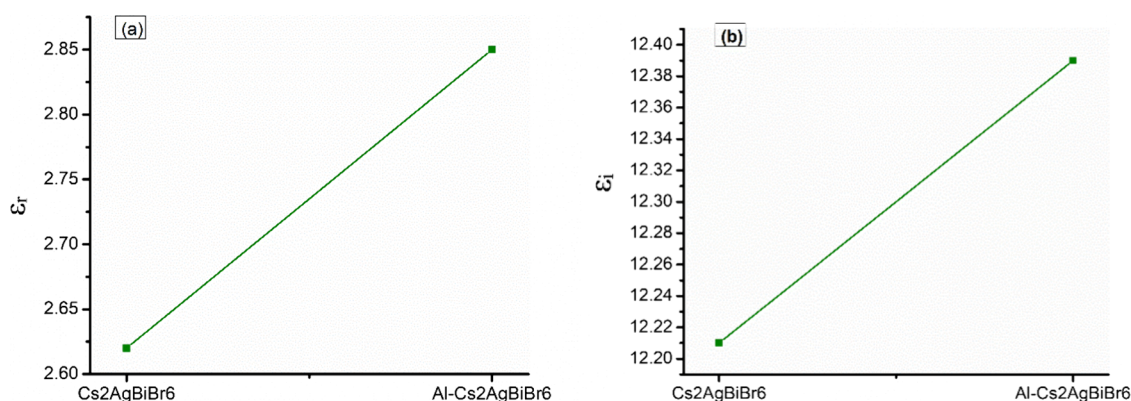
Figure 4. (a) Real part of extinction coefficient ε_r and (b) imaginary part of extinction coefficient ε_i for undoped and doped Al−$Cs_2AgBiBr_6$.

the less electronegative metal to the more electronegative nonmetal, resulting in the formation of ions with opposite charges.[68−71] The relationship between the energy gap (E_g) and optical electronegativity (χ^*) in systems is as follows[72]:

$$E_g = 3.72(\Delta\chi*) \tag{8}$$

where $(\Delta\chi^*)$ represents the variation in optical electronegativity between the cation and the anion. This equation suggests that E_g is directly proportional to the value of $\Delta\chi^*$, with a factor of 3.72. In the case of pure $Cs_2AgBiBr_6$, the value of $\Delta\chi^*$ is given as 0.513. In the doped $Cs_2AgBiBr_6$, the value of $\Delta\chi^*$ decreases to 0.48. As $\Delta\chi^*$ difference is 0.03, a nonpolar covalent bond is formed as shown in Figure 3b. Covalent bonds in double perovskite solar cells are essential for enhancing the material's structural stability. These bonds establish strong connections among the component atoms, which help maintain the integrity of the crystal structure. The presence of covalent bonds in double perovskite solar cells serves multiple purposes, including exerting influence on electronic properties, promoting efficient charge transport, and enabling engineering of the material's attributes. All of these factors collectively enhance the photovoltaic performance of the solar cell, making it more efficient in converting sunlight into electricity.[73−75]

The extinction coefficient (k) is a measure of the efficiency with which a substance absorbs light at a particular wavelength. It is an intrinsic property that relies on the atomic and chemical structural composition of the isolated sequences.[76] In the context of the LFHDP, k is determined using the provided mathematical equation[55]:

$$k = n/\Delta\chi^{*\gamma} \tag{9}$$

where the value of "γ" is −0.32 as by calculating the value of k for pristine $Cs_2AgBiBr_6$ was 2.221, but for the doped Al, the 'k' value becomes 2.220 shown by the graph in Figure 3b. Doping with 5% Al results in a decrease in the value of 'k'. This reduction in 'k' may indicate a decrease in optical losses due to surface optical dispersion, an increase in carrier concentration, and reduced surface roughness. The optical characteristics of semiconductor materials can be described using the complex dielectric function (ε)[77]:

$$\varepsilon = \varepsilon_r + i\varepsilon_i \tag{10}$$

where ε_r represents the real part, and ε_i stands for the imaginary component of the dielectric constant, which are represented in terms of "n' and 'k" as[42,77]:

$$\varepsilon_r = n^2 + k^2 \tag{11}$$

$$\varepsilon_i = 2nk \tag{12}$$

The real part of the ε indeed demonstrates the degree to which materials polarize when exposed to electromagnetic fields or incident light. The ε_i value is associated with electron transitions, which rely on electron movements between the conduction and valence bands. The ε_i value of the dielectric function is of significant importance for any material. It functions as a connection between the microphysical mechanisms involved in interband transitions and the electronic arrangement within the solid. This facilitates a deeper understanding of the solid's energy band structure and various spectral information. The ε_r and ε_i values of the dielectric constant increase with doping. In the undoped material, the ε_r and ε_i values are 2.62 and 12.21, respectively, while in the doped material, they rise to 2.85 and 12.39 as shown in Figure 4a,b, indicating the impact of doping on these dielectric properties. The observation that the values of the ε_r part are higher compared to the ε_i value in Al-doped $Cs_2AgBiBr_6$ films indicates an increase in the real part of the dielectric constant in these thin films due to Al doping. It may be possible that such an increase is likely a result of an enhanced electric flux density in the $Cs_2AgBiBr_6$ thin films caused by the introduction of Al. Consequently, optical conductivity is improved with Al doping, leading to increased electronic transfers through the films.[61,78]

3.3. J−V Curve. Using the J−V curve in Figure 5, the short-circuit current density (J_{sc}), fill factor (FF), open-circuit voltage (V_{oc}), and efficiency η (%) of $Cs_2AgBiBr_6$-based solar cell and Al-doped $Cs_2AgBiBr_6$ solar cell are determined, and the calculated values are given in Table 1.

When the electrodes of a solar cell are directly linked, J_{sc} represents the electrical current that flows through the external circuit. A solar cell's J_{sc} value is influenced by the photon flux that the incident light produces, which is established by the light's spectral makeup. The word 'J_{sc}' is frequently used to refer to the highest current output that a solar cell can produce. For pure $Cs_2AgBiBr_6$, J_{sc} is 5.01 mA/cm^2 in its undoped state and after Al doping, it increases to 5.29 mA cm^{-2}. Numerous variables affect J_{sc}, such as the chance of electron collection, optical characteristics, incident light intensity, and the incident light's spectral composition. A decrease in the bandgap is frequently linked to an increase in J_{sc}, which raises the material's electron density.[79−81]
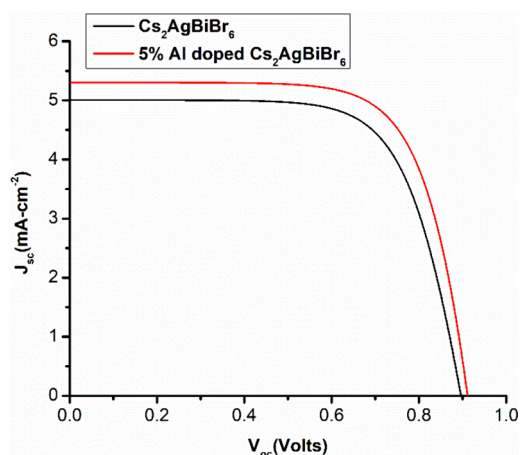
Figure 5. $J-V$ curve of pure and Al-doped solar cell.

Table 1. Solar Cell Parameters of Pure and Al-Doped Cs₂AgBiBr₆

samples	J_{sc} (mA/cm²)	V_{oc} (V)	FF	efficiency (η%)
Cs₂AgBiBr₆	5.01	0.89	0.67	3.02
5% Al doped	5.29	0.91	0.71	3.40

V_{oc} is one of the most critical parameters in determining the PCE of organic solar cells. V_{oc} for the doped Al is 0.91 V, while for the undoped, it becomes 0.89 V. The energy difference between the conduction band (CB) of the electron acceptor and the valence band (VB) of the electron donor is the primary source of the V_{oc} value. In the case of Al doping, the stronger interaction between Al-3p and Ag-5s states widens the CB, causing the density of states to shift toward lower energy levels. As a result, for the Al-doped material, the Fermi level moves upward into the CB, giving rise to the formation of an n-type semiconductor and making optical transitions more accessible. This shift in the Fermi level and the easier optical transition account for the increase in the V_{oc} value.[82−84] The FF of a solar cell is calculated by dividing the maximum power output (P_{max}) by $V_{oc} \times J_{sc}$[85,86]:

$$\text{FF} = \frac{P_{max}}{J_{sc} \times V_{oc}} \tag{13}$$

where $P_{max} = (J_{max} \times V_{max})$. The FF value of pure was 0.67, but after doping, its value increased to 0.71. The FF is indeed influenced by the recombination rate within a solar cell. A higher FF often indicates a reduced recombination rate, signifying a better cell performance. It is possible that the doping of Al has a role in reducing the recombination of electron−hole pairs, which in turn leads to the presence of more free electrons in the CB. This, in turn, lowers electrical resistance and increases the FF value[87]:

$$\eta = \frac{V_{oc} \times J_{sc} \times \text{FF}}{P_{in}} \tag{14}$$

To compare the performance of various solar cells, efficiency is the most frequently employed parameter. The efficiency of LFHDPs for undoped was 3.02%, and for doped, it became 3.40%, which was calculated through eq 14. This improvement in efficiency can be attributed to the increase in several key parameters, including J_{sc}, V_{oc}, and FF. Due to this, LFHDP

cells are more effective at converting incident light into electrical power.[81,88]

4. CONCLUSIONS

The perovskite solar cells using Cs₂AgBiBr₆ with and without Al doping were fabricated by a sol−gel spin-coating method. It was concluded that the doping of Al in Cs₂AgBiBr₆ effects substantially on its structural, optical, and photovoltaic properties. The structural properties were clarified from the lattice parameter, dislocation line density, crystal size, d-spacing, and the volume of particles, obtained based on the XRD pattern. In addition, the optical properties were calculated from UV−vis spectroscopy, which are bandgap, electronegativity, extinction coefficient, and dielectric constant. The peaks in the XRD were shifted, which confirms the Al presence. The increase in intensity of the peaks shows its crystallinity. The grain size was increased, and E_g decreased with Al doping. The $J-V$ curve showed that the device performance for pristine Cs₂AgBiBr₆ was 5.01 mA/cm² of J_{sc}, 0.89 V of V_{oc}, 0.67 of FF, and 3.02% of the efficiency of a double perovskite solar cell. The calculated parameters for Al-doped material are extracted from the $J-V$ graph, which revealed 5.29 mA/cm² of J_{sc}, 0.91 V of V_{oc}, and 0.71 of FF. Overall, the efficiency was increased by Al doping to 3.40% which is 12.5% greater than that of the pure Cs₂AgBiBr₆ thin film. It was concluded that this study not only shows a notable improvement in the solar cell performance but is the first to comprehensively describe the aforementioned properties of Cs₂AgBiBr₆ and Al-doped Cs₂AgBiBr₆ as well.

■ AUTHOR INFORMATION

Corresponding Authors

Muhammad Iftikhar Khan − *Department of Physics, The University of Lahore, Lahore 53700, Pakistan;* orcid.org/0009-0005-0584-053X; Email: muhammad.iftikhar@phys.uol.edu.pk

Jeong Ryeol Choi − *School of Electronic Engineering, Kyonggi University, Suwon, Gyeonggi-do 16227, Republic of Korea;* Email: choiardor@hanmail.net

Authors

Asad Ullah − *Department of Physics, The University of Lahore, Lahore 53700, Pakistan*

Ihtisham-ul-haq − *Department of Physics, The University of Lahore, Lahore 53700, Pakistan*

Badriah S. Almutairi − *Department of Physics, College of Science, Princess Nourah bint Abdulrahman University, Riyadh 11671, Saudi Arabia*

Dalil Bulayis N. AlResheedi − *Department of Physics, College of Science, Qassim University, Buraidah 51452, Saudi Arabia*

Complete contact information is available at:
https://pubs.acs.org/10.1021/acsomega.3c10388

Notes

The authors declare no competing financial interest.

(PNURSP2024R327), Princess Nourah bint Abdulrahman University, Riyadh, Saudi Arabia.

■ REFERENCES

(1) Qureshi, F.; Yusuf, M.; Kamyab, H.; Vo, D.-V. N.; Chelliapan, S.; Joo, S.-W.; Vasseghian, Y. Latest eco-friendly avenues on hydrogen production towards a circular bioeconomy: Currents challenges, innovative insights, and future perspectives. *Renewable and Sustainable Energy Reviews* **2022**, *168*, No. 112916.

(2) Huang, Z.; Luo, P.; Wu, Q.; Zheng, H. Constructing one-dimensional mesoporous carbon nanofibers loaded with NaTi2 (PO4) 3 nanodots as novel anodes for sodium energy storage. *J. Phys. Chem. Solids* **2022**, *161*, No. 110479.

(3) Kumar, A.; Singh, S.; Mohammed, M. K.; Shalan, A. E. Effect of 2D perovskite layer and multivalent defect on the performance of 3D/2D bilayered perovskite solar cells through computational simulation studies. *Sol. Energy* **2021**, *223*, 193−201.

(4) Al-mousoi, A.; Mehde, M.; Al-gebori, A. Annealing temperature effects on the performance of the perovskite solar cells. In *IOP Conference Series: Materials Science and Engineering*; IOP Publishing, 2020; Vol. *757*, p. 012039.

(5) Correa-baena, J.-P.; Saliba, M.; Buonassisi, T.; Grätzel, M.; Abate, A.; Tress, W.; Hagfeldt, A. Promises and challenges of perovskite solar cells. *Science* **2017**, *358* (6364), 739−744.

(6) Ghosh, S.; Shankar, H.; Kar, P. Recent developments of lead-free halide double perovskites: a new superstar in the optoelectronic field. *Materials Advances* **2022**, *3* (9), 3742−3765.

(7) Hu, F.; Mou, S.; Wei, S.; Qiu, L.; Hu, H.; Zhou, H. Research on the evolution of China's photovoltaic technology innovation network from the perspective of patents. *Energy Strategy Rev.* **2024**, *51*, No. 101309.

(8) Lei, H.; Hardy, D.; Gao, F. Lead-free double perovskite Cs2AgBiBr6: fundamentals, applications, and perspectives. *Adv. Funct. Mater.* **2021**, *31* (49), No. 2105898.

(9) Wang, M.; Jiang, C.; Zhang, S.; Song, X.; Tang, Y.; Cheng, H.-M. Reversible calcium alloying enables a practical room-temperature rechargeable calcium-ion battery with a high discharge voltage. *Nature Chem.* **2018**, *10* (6), 667−672.

(10) Khan, M.; Hussain, S.; Subhani, W. S.; Ammami, M.; Shahid, W.; Ali, R. Tungsten dopant incorporation for bandgap and type engineering of perovskite crystals. *Phys. Scr.* **2023**, *98* (9), No. 095517.

(11) Bhaumik, S.; Ray, S.; Batabyal, S. K. Recent advances of lead-free metal halide perovskite single crystals and nanocrystals: synthesis, crystal structure, optical properties, and their diverse applications. *Materials today chemistry* **2020**, *18*, No. 100363.

(12) Kojima, A.; Teshima, K.; Shirai, Y.; Miyasaka, T. Organometal halide perovskites as visible-light sensitizers for photovoltaic cells. *Journal of the American chemical society* **2009**, *131* (17), 6050−6051.

(13) Yang, W. S.; Noh, J. H.; Jeon, N. J.; Kim, Y. C.; Ryu, S.; Seo, J.; Seok, S. I. High-performance photovoltaic perovskite layers fabricated through intramolecular exchange. *Science* **2015**, *348* (6240), 1234−1237.

(14) Karmakar, A.; Dodd, M. S.; Agnihotri, S.; Ravera, E.; Michaelis, V. K. Cu (II)-doped Cs2SbAgCl6 double perovskite: A lead-free, low-bandgap material. *Chem. Mater.* **2018**, *30* (22), 8280−8290.

(15) Li, X.; Aftab, S.; Abbas, A.; Hussain, S.; Aslam, M.; Kabir, F.; Abd-rabboh, H. S.; Hegazy, H.; Xu, F.; Ansari, M. Z. Advances in mixed 2D and 3D perovskite heterostructure solar cells: a comprehensive review. *Nano Energy* **2023**, *118*, 108979.

(16) Wang, M.; Wang, W.; Ma, B.; Shen, W.; Liu, L.; Cao, K.; Chen, S.; Huang, W. Lead-free perovskite materials for solar cells. *Nano-Micro Lett.* **2021**, *13*, 62.

(17) Mu, S.; Liu, Q.; Kidkhunthod, P.; Zhou, X.; Wang, W.; Tang, Y. Molecular grafting towards high-fraction active nanodots implanted in N-doped carbon for sodium dual-ion batteries. *Natl. Sci. Rev.* **2021**, *8* (7), No. nwaa178.

(18) Tailor, N. K.; Listorti, A.; Colella, S.; Satapathi, S. Lead-Free Halide Double Perovskites: Fundamentals, Challenges, and Photovoltaics Applications. *Adv. Mater. Technol.* **2023**, *8* (1), No. 2200442.

(19) Kung, P.-K.; Li, M.-H.; Lin, P.-Y.; Jhang, J.-Y.; Pantaler, M.; Lupascu, D. C.; Grancini, G.; Chen, P. Lead-free double perovskites for perovskite solar cells. *Solar RRL* **2020**, *4* (2), No. 1900306.

(20) Sekar, K.; Marasamy, L.; Mayarambakam, S.; Hawashin, H.; Nour, M.; Bouclé, J. Lead-free, formamidinium germanium-antimony halide (FA 4 GeSbCl 12) double perovskite solar cells: the effects of band offsets. *RSC Adv.* **2023**, *13* (36), 25483−25496.

(21) Kale, A. J.; Chaurasiya, R.; Dixit, A. Photovoltaic characteristics of ultrathin Cs2CuBiCl6 halide double perovskite based solar cell: theoretical studies. *Optik* **2023**, *281*, No. 170820.

(22) Longo, G.; Mahesh, S.; Buizza, L. R.; Wright, A. D.; Ramadan, A. J.; Abdi-jalebi, M.; Nayak, P. K.; Herz, L. M.; Snaith, H. J. Understanding the performance-limiting factors of Cs2AgBiBr6 double-perovskite solar cells. *ACS Energy Letters* **2020**, *5* (7), 2200−2207.

(23) Yadav, S. C.; Srivastava, A.; Manjunath, V.; Kanwade, A.; Devan, R. S.; Shirage, P. M. Properties, performance and multi-dimensional applications of stable lead-free Cs2AgBiBr6 double perovskite. *Mater. Today Phys.* **2022**, *26*, No. 100731.

(24) Huang, Z.; Luo, P.; Jia, S.; Zheng, H.; Lyu, Z. A sulfur-doped carbon-enhanced Na3V2 (PO4) 3 nanocomposite for sodium-ion storage. *J. Phys. Chem. Solids* **2022**, *167*, No. 110746.

(25) Lu, L.; Wu, W.; Gao, Y.; Pan, C.; Yu, X.; Zhang, C.; Jin, Z. Study on current discrepancy and redistribution of HTS non-insulation closed-loop coils during charging/discharging and subsequent transient process toward steady-state operation. *Supercond. Sci. Technol.* **2022**, *35* (9), No. 095001.

(26) Yang, S.; Huang, Z.; Hu, Q.; Zhang, Y.; Wang, F.; Wang, H.; Shu, Y. Proportional optimization model of multiscale spherical BN for enhancing thermal conductivity. *ACS Applied Electronic Materials* **2022**, *4* (9), 4659−4667.

(27) Greul, E.; Petrus, M. L.; Binek, A.; Docampo, P.; Bein, T. Highly stable, phase pure Cs 2 AgBiBr 6 double perovskite thin films for optoelectronic applications. *Journal of Materials Chemistry A* **2017**, *5* (37), 19972−19981.

(28) Jiang, C.; Deng, Z.; Liu, B.; Li, J.; Han, Z.; Ma, Y.; Wu, D.; Maeda, H.; Ma, Y. Spin−Orbit-Engineered Selective Transport of Photons in Plasmonic Nanocircuits with Panda-Patterned Transporters. *ACS Photonics* **2022**, *9* (9), 3089−3093.

(29) Pantaler, M.; Olthof, S.; Meerholz, K.; Lupascu, D. C. Bismuth-Antimony mixed double perovskites Cs2AgBi1-xSbxBr6 in solar cells. *MRS Advances* **2019**, *4* (64), 3545−3552.

(30) Huang, Z.; Zhang, Y.; Wang, H.; Li, J. Improved electrical resistivity-temperature characteristics of oriented hBN composites for inhibiting temperature-dependence DC surface breakdown. *Appl. Phys. Lett.* **2023**, *123*, 103501.

(31) Zhang, Y.; Liu, X.; Song, M.; Qin, Z. Tuning the Red-to-Green-Upconversion Luminescence Intensity Ratio of Na3ScF6:20% Yb3+, 2% Er3+ Particles by Changes in Size. *Materials* **2023**, *16* (6), 2247.

(32) Azizah, N. m.; Muhammady, S.; Purbayanto, M. A. K.; Nurfani, E.; Winata, T.; Sustini, E.; Widita, R.; Darma, Y. Influence of Al doping on the crystal structure, optical properties, and photodetecting performance of ZnO film. *Progress in Natural Science: Materials International* **2020**, *30* (1), 28−34.

(33) Khlayboonme, S. T.; Thowladda, W. Impact of Al-doping on structural, electrical, and optical properties of sol-gel dip coated ZnO: Al thin films. *Materials Research Express* **2021**, *8* (7), No. 076402.

(34) Mishra, P. N.; Mishra, P. K.; Pathak, D. The influence of Al doping on the optical characteristics of ZnO nanopowders obtained by the low-cost sol-gel method. *Chemistry* **2022**, *4* (4), 1136−1146.

(35) Wai, H. S.; Li, C. Effect of aluminum doping ratios on the properties of aluminum-doped zinc oxide films deposited by mist chemical vapor deposition method applying for photocatalysis. *Nanomaterials* **2022**, *12* (2), 195.

(36) Zhang, X.; Tang, Y.; Zhang, F.; Lee, C.-S. A novel aluminum—graphite dual-ion battery. *Adv. Energy Mater.* **2016**, *6* (11), No. 1502588.

(37) El-henawey, M.; Hossain, I. M.; Zhang, L.; Bagheri, B.; Kottokkaran, R.; Dalal, V. L. Influence of grain size on the photostability of perovskite solar cells. *Journal of Materials Science: Materials in Electronics* **2021**, *32*, 4067—4075.

(38) Adnan, M.; Usman, M.; Ali, S.; Javed, S.; Islam, M.; Akram, M. A. Aluminum Doping Effects on Interface Depletion Width of Low Temperature Processed ZnO Electron Transport Layer-Based Perovskite Solar Cells. *Frontiers in Chemistry* **2022**, *9*, No. 795291.

(39) Kruszyńska, J.; Ostapko, J.; Ozkaya, V.; Surucu, B.; Szawcow, O.; Nikiforow, K.; Hołdyński, M.; Tavakoli, M. M.; Yadav, P.; Kot, M. Atomic Layer Engineering of Aluminum-Doped Zinc Oxide Films for Efficient and Stable Perovskite Solar Cells. *Adv. Mater. Interfaces* **2022**, *9* (17), No. 2200575.

(40) Murgulov, V.; Schweinle, C.; Daub, M.; Hillebrecht, H.; Fiederle, M.; Dědič, V.; Franc, J. Double perovskite Cs 2 AgBiBr 6 radiation sensor: synthesis and characterization of single crystals. *J. Mater. Sci.* **2022**, *57*, 2758—2774.

(41) Abdelsamie, M.; Cruse, K.; Tamura, N.; Ceder, G.; Sutter-fella, C. M. Impact of processing conditions on the film formation of lead-free halide double perovskite Cs 2 AgBiBr 6. *Journal of Materials Chemistry A* **2022**, *10* (37), 19868—19880.

(42) Khan, M.; Bhatti, K.; Qindeel, R.; Althobaiti, H. S.; Alonizan, N. Structural, electrical and optical properties of multilayer TiO2 thin films deposited by sol—gel spin coating. *Results in physics* **2017**, *7*, 1437—1439.

(43) Khan, M. I.; Yasmin, S.; Alwadai, N.; Irfan, M.; Albalawi, H.; Almuqrin, A. H.; Almoneef, M. M.; Iqbal, M. Bi and Sn Doping Improved the Structural, Optical and Photovoltaic Properties of MAPbI3-Based Perovskite Solar Cells. *Materials* **2022**, *15* (15), 5216.

(44) Fang, F.; Li, H.; Fang, S.; Zhou, B.; Huang, F.; Ma, C.; Wan, Y.; Jiang, S.; Wang, Y.; Tian, B. 2D Cs2AgBiBr6 with Boosted Light—Matter Interaction for High-Performance Photodetectors. *Adv. Opt. Mater.* **2021**, *9* (9), No. 2001930.

(45) Sharma, N.; Kumar, S. Effect of Ag Doping on Properties of Al—Doped ZnO Nanoparticles Varies as Zn1-X-YAgxALYO. *Mater. Sci. Res. India* **2017**, *14*, 146.

(46) Khan, M.; Shehzad, A.; Farooq, W.; Arfan, M.; Hasan, M.; Atif, M.; Hanif, A. 900 keV Au ions implantation effect on the efficiency of dye sensitized solar cells. *Results Phys.* **2019**, *14*, No. 102425.

(47) Bano, S.; Khan, M.; Albalawi, H.; Ul islam, G.; Siddique, M.; Ahmad, T.; Alkhaldi, H.; Ahson, R.; Hussain, S. Effect of Cd doping on the structural, optical, and photovoltaic properties of SnS films. *J. Mater. Res. Technol.* **2022**, *19*, 1982—1992.

(48) Sivakumar, P.; Akkera, H. S.; Reddy, T. R. K.; Bitla, Y.; Ganesh, V.; Kumar, P. M.; Reddy, G. S.; Poloju, M. Effect of Ti doping on structural, optical and electrical properties of SnO2 transparent conducting thin films deposited by sol-gel spin coating. *Opt. Mater.* **2021**, *113*, No. 110845.

(49) Hussain, S.; Alwadai, N.; Khan, M. I.; Irfan, M.; Albalawi, H.; Almuqrin, A. H.; Almoneef, M. M.; Iqbal, M. The effect of 600 keV Ag ion irradiation on the structural, optical, and photovoltaic properties of MAPbBr3 films for perovksite solar cell applications. *Materials* **2022**, *15* (15), 5299.

(50) Alsaad, A. M.; Ahmad, A. A.; Al-bataineh, Q. M.; Bani-salameh, A. A.; Abdullah, H. S.; Qattan, I. A.; Albataineh, Z. M.; Telfah, A. D. Optical, structural, and crystal defects characterizations of dip synthesized (Fe-Ni) Co-doped ZnO thin films. *Materials* **2020**, *13* (7), 1737.

(51) Amroun, M.; Salim, K.; Kacha, A.; Khadraoui, M. Effect of TM (TM= Sn, Mn, Al) doping on the physical properties of ZnO thin films grown by spray pyrolysis technique: a comparative study. *Int. J. Thin. Film. Sci. Technol.* **2020**, *9* (1), 7—19.

(52) Haq, I.; Khan, M.; Irfan, M.; Fatima, M.; Somaily, H.; Elqahtani, Z. M.; Alwadai, N. Increase the current density and reduce the defects of ZnO by modification of the band gap edges with Cu ions implantation for efficient, flexible dye-sensitized solar cells

(FDSSCs). *Ceram. Int.* **2023**, *49*, 29622 DOI: 10.1016/j.ceramint.2023.06.188.

(53) Burns, A.; Hayes, G.; Li, W.; Hirvonen, J.; Demaree, J. D.; Shah, S. I. Neodymium ion dopant effects on the phase transformation in sol—gel derived titania nanostructures. *Materials Science and Engineering: B* **2004**, *111* (2—3), 150—155.

(54) Thawarkar, S.; Rondiya, S. R.; Dzade, N. Y.; Khupse, N.; Jadkar, S. Experimental and Theoretical Investigation of the Structural and Opto-electronic Properties of Fe-Doped Lead-Free Cs2AgBiCl6 Double Perovskite. *Chemistry—A. European Journal* **2021**, *27* (26), 7408—7417.

(55) Khan, M. I.; Mukhtar, A.; Alwadai, N.; Irfan, M.; Haq, I.-U.; Albalawi, H.; Almuqrin, A. H.; Almoneef, M. M.; Iqbal, M. Improving the structural, optical and photovoltaic properties of Sb-and Bi-Co-doped MAPbBr3 perovskite solar cell. *Coatings* **2022**, *12* (3), 386.

(56) Khan, M.; Ali, S.; Alwadai, N.; Irfan, M.; Albalawi, H.; Almuqrin, A. H.; Almoneef, M. M.; Iqbal, M. Structural, electrical and optical properties of hetrostructured MoS2/ZnO thin films for potential perovskite solar cells application. *J. Mater. Res. Technol.* **2022**, *20*, 1616—1623.

(57) Yang, J.; Zhang, P.; Wei, S.-H. Band structure engineering of Cs2AgBiBr6 perovskite through order—disordered transition: A first-principle study. *journal of physical chemistry letters* **2018**, *9* (1), 31—35.

(58) Zheng, X.; Colegrove, E.; Duenow, J.; Moseley, J.; Metzger, W. Roles of bandgrading, lifetime, band alignment, and carrier concentration in high-efficiency CdSeTe solar cells. *J. Appl. Phys.* **2020**, *128* (5), No. 053102, DOI: 10.1063/5.0013726.

(59) Guo, H.; Meng, R.; Wang, G.; Wang, S.; Wu, L.; Li, J.; Wang, Z.; Dong, J.; Hao, X.; Zhang, Y. Band-gap-graded Cu 2 ZnSn (S, Se) 4 drives highly efficient solar cells. *Energy Environ. Sci.* **2022**, *15* (2), 693—704.

(60) Khan, M.; Farooq, W.; Saleem, M.; Bhatti, K.; Atif, M.; Hanif, A. Phase change, band gap energy and electrical resistivity of Mg doped TiO2 multilayer thin films for dye sensitized solar cells applications. *Ceram. Int.* **2019**, *45* (17), 21436—21439.

(61) Chen, H.; Qu, Y.; Sun, L.; Peng, J.; Ding, J. Band structures and optical properties of Ag and Al co-doped ZnO by experimental and theoretic calculation. *Physica E: Low-dimensional Systems and Nanostructures* **2019**, *114*, No. 113602.

(62) Feng, X.; Sun, L.; Wang, W.; Zhao, Y.; Shi, J.-W. Construction of CdS@ ZnO core—shell nanorod arrays by atomic layer deposition for efficient photoelectrochemical H2 evolution. *Sep. Purif. Technol.* **2023**, *324*, No. 124520.

(63) Hadia, N.; Mohamed, H. A.-H. Characteristics and optical properties of MgO nanowires synthesized by solvothermal method. *Materials Science in Semiconductor Processing* **2015**, *29*, 238—244.

(64) Ravindra, N.; Ganapathy, P.; Choi, J. Energy gap—refractive index relations in semiconductors—An overview. *Infrared physics & technology* **2007**, *50* (1), 21—29.

(65) Khan, M.; Naeem, M.; Mustafa, G. M.; Abubshait, S. A.; Mahmood, A.; Al-masry, W.; Al-garadi, N. Y.; Ramay, S. M. Synthesis and characterization of Co and Ga co-doped ZnO thin films as an electrode for dye sensitized solar cells. *Ceram. Int.* **2020**, *46* (17), 26590—26597.

(66) Ali, M. A.; Alshgari, R. A.; Awadh bahajjaj, A. A.; Sillanpää, M. The study of new double perovskites K2AgAsX6 (X= Cl, Br) for energy-based applications. *J. Taibah Univ. Sci.* **2023**, *17* (1), No. 2170680.

(67) Sta, I.; Jlassi, M.; Hajji, M.; Boujmil, M.; Jerbi, R.; Kandyla, M.; Kompitsas, M.; Ezzaouia, H. Structural and optical properties of TiO 2 thin films prepared by spin coating. *J. Sol-Gel Sci. Technol.* **2014**, *72*, 421—427.

(68) Hinze, J.; Jaffe, H. H.; Electronegativity, I. Electronegativity. I. Orbital electronegativity of neutral atoms. *J. Am. Chem. Soc.* **1962**, *84* (4), 540—546.

(69) Reddy, R.; Ahammed, Y. N.; Gopal, K. R.; Azeem, P. A.; Rao, T.; Reddy, P. M. Optical electronegativity, bulk modulus and electronic polarizability of materials. *Opt. Mater.* **2000**, *14* (4), 355—358.

(70) Huang, Q.-M.; Hu, C.-L.; Yang, B.-P.; Tang, R.-L.; Chen, J.; Fang, Z.; Li, B.; Mao, J.-G. Ba2 [MoO3 (OH)(IO3) 2] IO3: a promising SHG material featuring a Λ-shaped functional motif achieved by universal mono-site substitution. *Chem. Mater.* **2020**, *32* (15), 6780−6787.

(71) Agarwal, A.; Pettersson, F.; Singh, A.; Kong, C. S.; Saxen, H.; Rajan, K.; Iwata, S.; Chakraborti, N. Identification and optimization of AB2 phases using principal component analysis, evolutionary neural nets, and multiobjective genetic algorithms. *Materials and Manufacturing Processes* **2009**, *24* (3), 274−281.

(72) Reddy, R.; Gopal, K. R.; Narasimhulu, K.; Reddy, L. S. S.; Kumar, K. R.; Reddy, C. K.; Ahmed, S. N. Correlation between optical electronegativity and refractive index of ternary chalcopyrites, semiconductors, insulators, oxides and alkali halides. *Opt. Mater.* **2008**, *31* (2), 209−212.

(73) Pan, S.; Zhang, Y.; Teng, X.; Li, G.; Li, L. Optical properties of nitrogen-doped SnO2 films: Effect of the electronegativity on refractive index and band gap. *J. Appl. Phys.* **2008**, *103* (9), No. 093103, DOI: 10.1063/1.2908197.

(74) Liu, K.; Rafique, S.; Musolino, S. F.; Cai, Z.; Liu, F.; Li, X.; Yuan, Y.; Bao, Q.; Yang, Y.; Chu, J. Covalent bonding strategy to enable non-volatile organic cation perovskite for highly stable and efficient solar cells. *Joule* **2023**, *7* (5), 1033−1050.

(75) Luo, Z.-Z.; Cai, S.; Hao, S.; Bailey, T. P.; Luo, Y.; Luo, W.; Yu, Y.; Uher, C.; Wolverton, C.; Dravid, V. P. Extraordinary role of Zn in enhancing thermoelectric performance of Ga-doped n-type PbTe. *Energy Environ. Sci.* **2022**, *15* (1), 368−375.

(76) Ubi, G. M.; Ikpeme, E. V.; Essien, I. S. Essentials of the COVID-19 coronavirus. In *Data Science for COVID-19*; Elsevier, 2022; pp. 1−25.

(77) Kanwal, S.; Khan, M.; Uzair, M.; Fatima, M.; Bukhari, M.; Saman, Z.; Elsaeedy, H.; Shahzad, U.; Elqahtani, Z. M.; Alwadai, N. A facile green approach to the synthesis of Bi2WO6@ V2O5 heterostructure and their photocatalytic activity evaluation under visible light irradiation for RhB dye removal. *Arab. J. Chem.* **2023**, *16* (5), No. 104685.

(78) Nion, M. G. M.; Kabir, M. H.; Mona, M. A.; Haque, M. J.; Shahariar, N.; Hafiz, M.; Rahman, M. Effect of Al doping on morphology and optical properties of spray pyrolized MgO thin films. *Results Mater.* **2021**, *12*, No. 100235.

(79) Roudgar-amoli, M.; Shariatinia, Z. Dye-sensitized solar cells with efficiencies exceeding 10% engineered based on La2MnTiO6 double perovskite and MOF-derived Cr2O3/C nanocomposites in bi-layered photoanodes. *Opt. Mater.* **2023**, *145*, No. 114456.

(80) Koster, L. J. A. *Device physics of donor/acceptor-blend solar cells*, 2007.

(81) Singh, K. J.; Sarkar, S. K. Highly efficient ARC less InGaP/ GaAs DJ solar cell numerical modeling using optimized InAlGaP BSF layers. *Optical and Quantum Electronics* **2012**, *43*, 1−21.

(82) Shintaku, N.; Hiramoto, M.; Izawa, S. Doping for controlling open-circuit voltage in organic solar cells. *J. Phys. Chem. C* **2018**, *122* (10), 5248−5253.

(83) Suo, Z.; Dai, J.; Gao, S.; Gao, H. Effect of transition metals (Sc, Ti, V, Cr and Mn) doping on electronic structure and optical properties of CdS. *Results in Physics* **2020**, *17*, No. 103058.

(84) Li, X.; Aftab, S.; Hussain, S.; Kabir, F.; Henaish, A.; Al-sehemi, A. G. Dimensional Diversity (0D, 1D, 2D, 3D) in Perovskite Solar Cells: Exploring the Potential of Mix-dimensional Integrations. *J. Mater. Chem. A* **2024**, *12*, 4421 DOI: 10.1039/D3TA06953B.

(85) Attia, A.; Hussain, S.; Khan, M.; Sadaf, A.; Seliem, A. F.; Mohammed, A. Y.; Ibrahim, M. M. Tuning the band gap edges of perovskite material by Cd doping for achieving high current density in perovskite solar cells. *Ceram. Int.* **2023**, *49* (12), 20465−20469.

(86) Hussain, S.; Khan, M.; Ghafoor, A.; Subhani, W. S.; Shahid, W.; Mahmoud, Z.; Elqahtani, Z. M.; Ercan, F.; Alwadai, N.; Iqbal, M. Understanding the influence of Cu ions implantation towards highly efficient MAPbBr3 perovskite solar cells. *Opt. Mater.* **2023**, *140*, No. 113806.

(87) Shahedi, Z.; Jafari, M. R. Synthesis Al complex and investigating effect of doped ZnO nanoparticles in the electrical and optical efficiency of OLEDS. *Appl. Phys. A: Mater. Sci. Process.* **2017**, *123*, 98.

(88) Amjad, M.; Khan, M. I.; Alwadai, N.; Irfan, M.; Albalawi, H.; Almuqrin, A. H.; Almoneef, M. M.; Iqbal, M. Photovoltaic properties of ZnO films Co-doped with Mn and La to enhance solar cell efficiency. *Nanomaterials* **2022**, *12* (7), 1057.